

Constraints on Thermal History of Mars from Depth of Pore Closure Below InSight

Szilárd Gyalay¹, Francis Nimmo¹, Ana-Catalina Plesa², and Mark Wieczorek³

¹University of California, Santa Cruz

²German Aerospace Center (DLR)

³Observatoire de la Côte d'Azur

Key Points:

- The depth of porosity in Mars' crust depends most on the maximum heat flux after pore generation.
- A seismic discontinuity at a depth of 8-11 km, as suggested by InSight, could be interpreted as the depth of porosity in the crust.
- If pores closed at 8-11 km depth, it indicates pores formed at least 4 billion years ago when heat flow was at least 60 mW m^{-2} .

Corresponding author: Szilárd Gyalay, sgyalay@ucsc.edu

Abstract

Planetary crusts undergo viscous closure of pores at depth; if the thickness of this porous layer can be measured, constraints on crustal thermal evolution can be derived. We apply a pore closure model developed for the Moon to Mars and take into account the geological processes that may alter the depth of this transition region. If the 8–11 km deep discontinuity in seismic wave speed detected by the InSight lander marks the base of the porous layer, the heat flux at the time the porosity was created must exceed 60 mW m^{-2} , probably indicating a time prior to 4 Ga.

Plain Language Summary

On long timescales, and with enough heat or pressure, rocks in the crust of a planet can flow. This viscous deformation allows the empty pore spaces in a rock to close up. The history of the temperature at depth plays an important role in how deep one may expect porosity to exist. One can use a computational model to calculate the thickness of this porous layer as a function of the crust's thermal history. If the InSight Mars lander detects the thickness of such a porous layer, we can estimate the necessary temperature structure of the Martian crust and when porosity in the crust was generated. From a potential measurement of this porous layer at around 10 kilometers thick, we predict the last significant pore formation event to have occurred at least 4 billion years ago.

1 Introduction

The porosity structure of the Martian crust is important for several reasons. It controls the crustal water carrying capacity (e.g. Clifford, 1993) and affects its near-surface thermal structure (Parmentier & Zuber, 2007). Furthermore, the porosity is an indication of the geological processes that have affected the crust, such as impact cratering, volcanism, and the emplacement of sediments. Less obviously, it contains a record of the thermal evolution of Mars, modulated by the history of crustal growth. Pores can close via plastic/viscous flow at a rate that is highly dependent on temperature (Hanna & Phillips, 2005); accordingly, if the depth to the base of the porous region can be established, the corresponding thermal structure may be deduced.

On the Moon, the presence of a porous layer roughly 40–85 km thick was identified using the very high resolution gravity data provided by GRAIL (Wieczorek et al., 2013; Besserer et al., 2014). The depth to the base of this layer was found to be consistent with models of viscous pore closure using simple lunar temperature structures (Wieczorek et al., 2013). In regions where the total crustal thickness is less than the depth of pore-closure, the uppermost mantle also likely maintains porosity (Wieczorek et al., 2013). Thermally-driven pore closure has also been modeled on icy satellites (e.g. Kossacki & Lorenz, 1996; Eluszkiewicz, 2004; Besserer et al., 2013) and on asteroids (e.g. Neumann et al., 2015; Gail et al., 2015). On the Moon, production of deep porosity was undoubtedly dominated by large impacts early in its history, and we will assume that the same is true for Mars.

Some studies of Martian aquifers (Clifford, 1993; Clifford & Parker, 2001) modeled porosity in Mars' crust as an exponential decay, scaled from a relationship hypothesized for the Moon, and observed in some geologic environments on Earth (e.g. Schmoker & Gautier, 1988). These relations focused on an elastic closure of pore space. At higher pressures or temperatures, rock deforms via ductile creep (Wong & Baud, 2012). On Earth, Manning and Ingebritsen (1999) interpret a drop in permeability at ~ 12 km depth due to ductile creep closing pores. Because of the lower gravity (and thus reduced elastic closure) on the Moon and Mars in conjunction with high heating early in their history, it is the latter process which we focus on in this work.

On the Moon, an apparent decay in seismic scattering with depth has been used to infer the depth to which fractured rocks extend (Gillet et al., 2017). In a similar fash-

64 ion, the recent emplacement of the InSight seismometer on the Martian surface provides
 65 the possibility of measuring the thickness of the porous layer. In this work, we carry out
 66 simple models of viscous pore closure for the Martian crust and show how the thickness
 67 of the porous layer can be related to the peak heat flux experienced. In Section 2, we
 68 review the mathematics of viscous pore closure. In section 3, we investigate the poten-
 69 tial confounding effects of geological processes of Mars' crust. In Section 4 we use a de-
 70 tected seismic discontinuity beneath InSight to quantify the thermal environment at the
 71 landing site when pore formation stopped, and thus determine *when* it stopped. We con-
 72 clude with Section 5.

73 2 Viscous Closure of Pores on Mars

74 We approach the problem in a similar fashion to Wicczorek et al. (2013) and ref-
 75 erences within (i.e. Fowler, 1985; Nimmo et al., 2003; Eluszkiewicz, 2004). How quickly
 76 the porosity ϕ closes over time t depends on the dynamic viscosity of the materials η and
 77 the overburden pressure P :

$$78 \quad \frac{\partial\phi}{\partial t} = -\phi \frac{P}{\eta}. \quad (1)$$

79 Pressure $P=\rho gz$ where ρ is crustal density, g is gravitational acceleration, and z is depth
 80 in the crust.

81 Under high pressures, viscosity does not depend on grain size but does depend on
 82 stress σ , rheological constants A and n , an activation energy Q , and the gas constant
 83 R :

$$84 \quad \eta = \frac{\sigma^{1-n}}{A} \exp\left(\frac{Q}{RT}\right). \quad (2)$$

85 We take this stress to be equal to the overburden pressure, $\sigma = P$. In reality there is
 86 a constant of proportionality of order unity in Equation 1 depending on the relationship
 87 of overburden pressure to the deviatoric stress, and the ratio of initial to current poros-
 88 ity (e.g. Eluszkiewicz, 2004). However, since the heat flux necessary for pore closure ul-
 89 timately depends on the logarithm of P (Section 2.3), neglecting this constant does not
 90 introduce significant errors. For instance, substituting $\sigma = 0.1P$ instead of $\sigma = P$ in
 91 Equation 1 depresses the depth of pore closure by ~ 2 km.

92 2.1 Constant Heat Flux Case

93 For the case of constant temperature, we solve Equation 1 to find ϕ relative to some
 94 initial porosity ϕ_0 after some elapsed time t as

$$95 \quad \phi = \phi_0 \exp\left(\frac{-Pt}{\eta}\right). \quad (3)$$

96 For an initially porous crust, we can use this equation to calculate how much the poros-
 97 ity at each depth has changed as a function of time. We assume pores have effectively
 98 closed when they reach a critical porosity that is a factor of e^2 less than the initial. The
 99 depth of the porous layer after some time is then limited by where porosity is still present;
 100 because of the strong temperature-dependence of viscosity, the transition to pore-free
 101 material is typically abrupt (less than a few km; Figure 1a). Because this transition is
 102 abrupt, the exact pore-closure criterion matters very little: one can take the character-
 103 istic criterion to be a factor of e or 10 and achieve nearly identical results.

104 For our nominal model, we use a gravitational acceleration of 3.7 m s^{-2} , an upper
 105 crustal density of 2800 kg m^{-3} , a rock thermal conductivity of $3.0 \text{ W m}^{-1} \text{ K}^{-1}$, no crustal
 106 heat production, and a constant surface temperature of 250 K. In this investigation we
 107 model Mars with both wet and dry diabase (as used in previous investigations of Mars,
 108 see e.g. Hanna & Phillips, 2005). For wet diabase, $Q = 276 \pm 14 \text{ kJ Mol}^{-1}$, $n = 3.05 \pm 0.15$,
 109 and $A = 6.12 \pm 3.06 \cdot 10^{-2} \text{ MPa}^{-n} \text{ s}^{-1}$ (Caristan, 1980). Caristan (1980) did not include

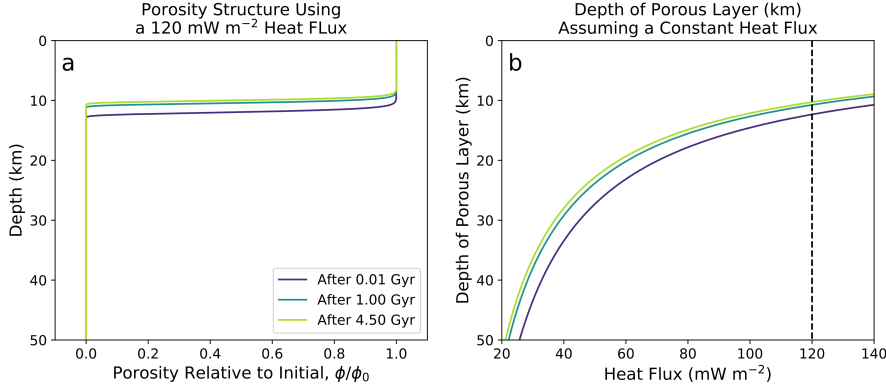


Figure 1. Panel a: Porosity structure after 10 Myr, 1 Gyr, and 4.5 Gyr for an assumed heat flux of 120 mW m^{-2} . Temperature structure at depth is calculated from Fourier’s law of thermal conduction for a surface temperature of 250 K, a thermal conductivity of $3 \text{ W m}^{-1} \text{ K}^{-1}$, and no crustal heat production. We use the rock rheology of wet diabase from Caristan (1980) without consideration for uncertainty. Porosity decreases from its initial value to 0 over a sharp interval of about 2 km.

Panel b: Depth of pore closure (where the porosity is reduced by a factor e^2 with respect to the initial value) as a function of heat flux. The dashed line illustrates the heat flux used for (a).

110 exact uncertainties, but noted that uncertainty in Q and n would not exceed 5%, and
 111 A could vary by a factor of 2. For dry diabase, $Q = 485 \pm 30 \text{ kJ Mol}^{-1}$, $n = 4.7 \pm 0.6$, and
 112 $A = 1.9 \pm 1.1 \cdot 10^2 \text{ MPa}^{-n} \text{ s}^{-1}$ (Mackwell et al., 1998). Some other parameter values are
 113 uncertain; in particular, thermal conductivity has a strong dependence on porosity as
 114 well as the contents of its pore space. We discuss the effect of these uncertainties fur-
 115 ther below and in Appendix A.

116 For the purpose of illustration, we assume a single rheology (wet diabase) and plot
 117 how the depth of pore closure changes through time for a range of constant heat fluxes
 118 in Figure 1b. Most pore closure happens in a short timespan. The depth of pore-closure
 119 over the age of the solar system, as shown in Figure 1b, is highly dependent on the as-
 120 sumed heat flux, ranging from depths of more than 50 km for low heat fluxes of about
 121 20 mW m^{-2} to about 10 km for heat fluxes in excess of 120 mW m^{-2} . Present-day heat
 122 fluxes on Mars are expected to be roughly 20 mW m^{-2} (see below), but would have been
 123 higher at earlier times. It is thus important to take into account the time-evolution of
 124 heat flux.

125 2.2 Decreasing Heat Flux Case

126 To investigate the effect of a changing heat flux, we make use of a suite of thermal
 127 evolution models developed by Plesa et al. (2018). The model uses a fully 3-D geome-
 128 try to model the thermal evolution and interior dynamics of Mars. We focus on their case
 129 110, as it represents an upper bound in terms of heat flux through time. Similar to most
 130 other cases of Plesa et al. (2018), case 110 uses a crustal thermal conductivity of $3 \text{ W m}^{-1} \text{ K}^{-1}$,
 131 latitudinal variations of the surface temperature leading to a surface temperature of 235 K
 132 at InSight location (Ohring & Mariano, 1968; Kieffer, 2013), and spatial variations of
 133 crustal thickness. The average crustal thickness of this model is 45 km and the crustal
 134 heat production rate is 20% higher than the value suggested by GRS (Hahn et al., 2011).
 135 The crustal heat production for case 110 decreases exponentially from an initial value
 136 of 331.1 pW kg^{-1} . We note that this case matches available geophysical, geological, and

137 petrological constraints (cf. supplementary material of Plesa et al., 2018). We use Equa-
 138 tion 1 to evolve the porosity forward in time, taking into account the effect of the chang-
 139 ing crustal temperature structure on the viscosity via Equation 2. Figure 2a shows the
 140 model surface heat flux through Martian history.

141 We begin the porosity evolution calculation at different points in Mars’s history.
 142 In this model, porosity is assumed to be present in the crust at some time t_0 , and then
 143 we compute the depth of pore closure. For each starting time point, we evolved Equa-
 144 tion 1 forward in time over either 10 Myr or 1 Gyr, showing that the results are not sen-
 145 sitive to the total elapsed time after initiation of pore closure (Figure 2b). Pore closure
 146 reaches shallower depths in cases when closure started earlier (when temperatures were
 147 higher). Because of the continuing decrease in heat flux, the pore closure depth is much
 148 more sensitive to the heat flux at the start of pore-closure than on the total duration of
 149 closure. In effect, the present-day depth of pore closure is a “fossil” signature of an an-
 150 cient heat flux. We accordingly are justified in using an analytical approach in which the
 151 initial, maximum heat flux is calculated from the present-day depth of pore closure.

152 2.3 Necessary/Maximum Heat Flux as a Function of Pore-Closure Depth

153 Assume that pores close at a critical porosity ϕ_C . Rearranging Equation 3, the crit-
 154 ical temperature T_C to close pores at some depth $z = (P/\rho g)$ (we account for uncer-
 155 tainty in the density due to porosity in Appendix A) after some time t is:

$$156 \quad T_C = \frac{Q/R}{\ln\left(\frac{tP^n A}{\ln(\phi_0/\phi_C)}\right)}. \quad (4)$$

157 This expression shows that the closure temperature is strongly dependent on the acti-
 158 vation energy Q and weakly dependent on the overburden pressure P and elapsed time
 159 t .

160 The temperature at depth is related to heat flux by Fourier’s law of thermal con-
 161 duction. We can thus determine the surface heat flux necessary to close pores at a cer-
 162 tain depth:

$$163 \quad F_C = \frac{k}{z} \left[\frac{Q/R}{\ln\left(\frac{tP^n A}{\ln(\phi_0/\phi_C)}\right)} - T_S + \frac{\rho H z^2}{2k} \right], \quad (5)$$

164 where T_S is the surface temperature, and H is the crustal heat production rate per unit
 165 mass. Because a decreasing heat flux results in little change in the depth of pore closure
 166 over time (assuming that no additional porosity is being generated, see Figure 2b), we
 167 can use a small elapsed time such as $t=10$ Myr and be confident that this results in the
 168 maximum heat flux a region can have experienced in its history.

169 3 Effects of Geology

170 Until now, we have made several simplifying assumptions in this analysis. We as-
 171 sumed pores close only viscously and neglected other ways of closing porosity such as
 172 cementation or volcanism. We also assume that the entire crust is initially porous, and
 173 that no new porosity is generated. Nonetheless, any subsurface region in which poros-
 174 ity is maintained can never have exceeded a given temperature since the most recent gen-
 175 eration of porosity, placing an upper bound on the heat flux. For the Moon, it is thought
 176 that early bombardment was the main source of porosity and that the decline in impacts
 177 greatly reduced subsequent pore generation (Wieczorek et al., 2013; Wahl et al., 2020).
 178 On Mars, the last events to generate significant porosity were likely the impacts that formed
 179 the Borealis Basin (>4.47 Ga) or Hellas, Isidis, and Argyre basins (~ 3.8 – 4.1 Ga) (Bottke
 180 & Andrews-Hanna, 2017).

181 In this section, we explore the regional geology near InSight and how it may affect
 182 our analysis. InSight landed in Elysium Planitia near the boundary of Mars’ crustal di-
 183 chotomy. From orbital data, InSight appears to have landed on a plain of early-Amazonian

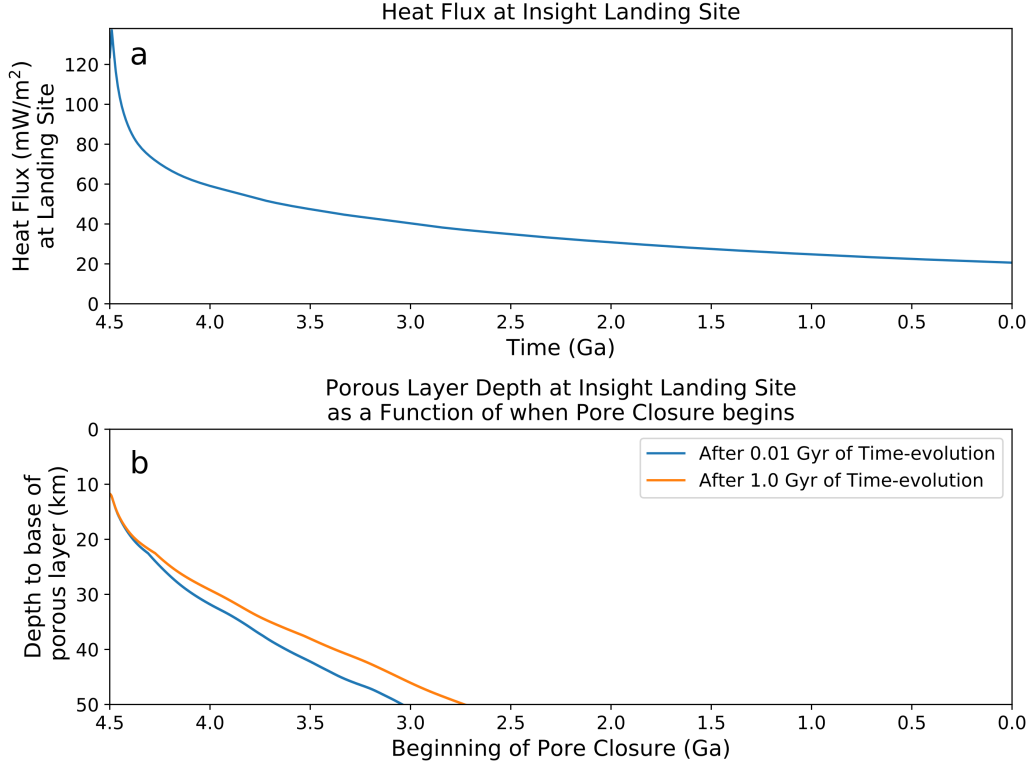


Figure 2. Panel a: Surface heat flux at InSight’s landing site, modeled through Martian history. This particular model is case 110 from Plesa et al. (2018), and uses a thermal conductivity $k=3 \text{ W m}^{-1} \text{ K}^{-1}$. The surface temperature in this Plesa et al. (2018) model was 235 K at the InSight landing site. Crustal heat production was initially 331.1 pW kg^{-1} and decreased exponentially to 59 pW kg^{-1} .

Panel b: To account for how a changing heat flux affects pore closure, we can no longer use Equation 3 over the total elapsed time. However, we may still employ this equation over short and successive time steps (we use 100 kyr). For example, if we begin pore closure at 4 Ga, we first assume the heat flux indicated in panel (a) for 4 Ga ($\sim 60 \text{ mW m}^{-2}$) and find porosity as a function of depth with Equations 2 and 3 after 100 kyr have elapsed. For the next time step, we use the heat flux 100 kyr after our start time and repeat the process. After the necessary number of time steps, we calculate the depth of the porous layer after 10 Myr and 1 Gyr of evolution from the corresponding start time. Due to the uncertainty in when pore-generation may have ended we allow the beginning of pore-closure to vary from 1.0-4.5 Ga. So as a function of this start time, we plot the depth of the porous layer after 10 Myr (blue line) and 1 Gyr (orange line) of heat flux evolution. We use the rock rheology of wet diabase from Caristan (1980). While porosity could continue into the upper mantle (cf. Wiczorek et al., 2013), we are primarily concerned with pore closure in the crust, as InSight has potentially detected pore closure at only $\sim 10 \text{ km}$ depth (Lognonné et al., 2020). As such, we truncate results at depths greater than a generous crustal thickness of 50 km.

184 or late-Hesperian (~ 3.0 Ga) lava flows 200-300 m thick, which overlie sedimentary rocks
 185 of Noachian age (~ 3.7 -4.1 Ga) (Pan et al., 2020). The sediments themselves may over-
 186 lie altered basaltic rocks that are compacted at depth (Smrekar et al., 2019). The sur-
 187 face geology at the landing site was well-predicted by the orbital data (Golombek et al.,
 188 2020). Initial analyses of the InSight seismic data using a seismic receiver function anal-
 189 ysis shows that there is a seismic discontinuity at 8-11 km depth (Lognonné et al., 2020).
 190 This discontinuity occurs within the crust of Mars, and potentially indicates the pres-
 191 ence of altered/fractured rocks to that depth (Lognonné et al., 2020).

192 We consider four geological phenomena that may affect the depth of pore-closure
 193 beneath the InSight landing site: sediment accumulation, emplacement of lava flows, ero-
 194 sion, and the presence of groundwater. If sedimentation occurred after maximum heat-
 195 ing, the extra overburden pressure it applies at depth would not cause additional com-
 196 paction but may effectively increase the depth to pore-closure by the thickness of the ad-
 197 ditional sediment. In addition, the sediments themselves would be expected to form with
 198 significant porosity (see Lewis et al., 2019). Lava flows would greatly increase the sur-
 199 face temperature, but the thermal anomaly will only propagate downwards to a depth
 200 comparable to the flow thickness, which is likely much less than the porous layer depth.
 201 Like sediment layers, this layer of lava would also increase the depth to pore-closure by
 202 the thickness of the deposit, and the lava flows would likely also contain some porosity
 203 (e.g. Rust et al., 1999, and references within). Erosion would remove at least some of
 204 the upper portion of the porous layer. However, there is little evidence for large scale
 205 erosive events in this region of Mars.

206 The presence of pore water will change the deviatoric stress. However, because of
 207 the large density contrast between water and rock, and the logarithmic dependence on
 208 P (Equation 5), this effect is negligible. Groundwater can also aqueously alter the min-
 209 eralogy via diagenesis (see Section 4 below). Most importantly for our study, an aquifer
 210 can affect the temperature structure of the crust and thus the depth to which pores close.
 211 The presence of liquid water in the pore space of Martian rock can lower the effective
 212 thermal conductivity of the rock (e.g. Hanna & Phillips, 2005)—increasing the thermal
 213 gradient and thus reducing the thickness of the porous layer. The thermal conductiv-
 214 ity of the Martian crust may be somewhere between 2 and 3 $\text{W m}^{-1} \text{K}^{-1}$ (e.g. Clauser
 215 & Huenges, 1995; Seipold, 1998) while water’s thermal conductivity is 0.57 $\text{W m}^{-1} \text{K}^{-1}$
 216 (Demming, 2002). A similar reduction in conductivity will arise if the pores are empty
 217 rather than water-filled. Uncertainty in the thermal conductivity has the largest effect
 218 on the uncertainty in the calculated maximum heat flux (see Appendix A).

219 Another possibility to consider is if water in the pore-space of the Martian crust
 220 is undergoing convection. This is important because convection decreases the thermal
 221 gradient—making the required heat flux to close pores at a given depth under the as-
 222 sumption of conduction (Equation 5) an underestimate. We can calculate whether the
 223 fluid would convect using the Rayleigh number for a fluid in a porous medium:

$$224 \quad Ra = \frac{\rho_w \alpha_w \Delta T g K l}{\phi \eta_w \kappa_w}, \quad (6)$$

225 where ρ_w is the density of water, α_w is the thermal expansivity of water, ΔT is the tem-
 226 perature difference across the change in depth, K is the permeability of the Martian re-
 227 golith, l is the lengthscale, ϕ is the porosity of the regolith, η_w is the viscosity of the wa-
 228 ter, and κ_w is the thermal diffusivity of water (Hewitt et al., 2014).

229 Although most of these variables are approximately known, the permeability and
 230 porosity of the crust are very uncertain. Hanna and Phillips (2005) estimated the ver-
 231 tical extent of potential Noachian aquifers by modeling the closure of pores in a man-
 232 ner resembling our approach. We approximate from their results, which derived a poros-
 233 ity that varied from 0.16 at the surface to 0.04 at a depth of ~ 10 km. They predicted
 234 the permeability of Martian regolith to vary from 10^{-11} m^2 at the surface to 10^{-15} m^2
 235 at depths of 5 km or more.

236 Taking an order of magnitude approach, we take $\rho_w = 10^3 \text{ kg m}^{-3}$, $\alpha_w = 10^{-4}$
 237 K^{-1} , $g = 4 \text{ m s}^{-2}$, $\eta_w = 10^{-3} \text{ Pa s}$, and $\kappa_w = 10^{-7} \text{ m}^2 \text{ s}^{-1}$. If we take a lengthscale

238 of 10 km, then let us take $K = 10^{-14} \text{ m}^2$ as a rough geometric mean of permeability
 239 (weighted more towards 10^{-15} m^2 as half the depth has that permeability). Similarly,
 240 let us assume a mean porosity of 0.1. If the surface of Mars is near the freezing temper-
 241 ature, then we may take $\Delta T = 100 \text{ K}$ as an upper bound. The Rayleigh number is then
 242 ~ 400 . We do not expect any flow below a Rayleigh number of $4\pi^2$, and then some tran-
 243 sition range above that (Hewitt et al., 2014). Depending on alterations in our order-of-
 244 magnitude assumptions, our simplified aquifer may be transitioning into convection. Since
 245 the effect of any such convection is to reduce the temperature gradient, our conductive
 246 solutions for the heat flux required to produce a particular porous layer depth (see be-
 247 low) will, if anything, be underestimates.

248 4 Application to InSight’s Landing Site

249 InSight has detected a discontinuity in seismic wave velocity 8-11 km below the sur-
 250 face, which may indicate the presence of altered or fractured rocks to that depth (Lognonné
 251 et al., 2020). We treat this as the transition from porous to compacted crust, but as a
 252 deeper probing of the Martian crust requires higher magnitude marsquakes, we cannot
 253 yet be sure if porosity actually continues to greater depths. Mineralogical changes can
 254 also cause seismic discontinuities, but the two transitions need not be independent: flu-
 255 ids fluxing through the permeable crust may cause diagenesis (e.g. Sun et al., 2019) and
 256 a corresponding reduction in seismic velocities, while leaving the impermeable crust un-
 257 changed. In effect, the porous/compacted rock boundary can become a mineralogical bound-
 258 ary that is detectable by InSight. In any event, if a different depth of pore closure is ul-
 259 timately detected, we can deduce the maximum heat flux experienced at the InSight land-
 260 ing site after pore generation.

261 In making our prediction for maximum heat flux experienced at the InSight land-
 262 ing site, we account for the uncertainty of each term in Equation 5 (see Appendix A).
 263 To account for a wide range of estimates of thermal conductivity of the Martian crust
 264 (with or without groundwater), we use separate thermal conductivities of $k = 1.5, 2.0,$
 265 and $3.0 \text{ W m}^{-1} \text{ K}^{-1}$. We use an average present-day temperature of 235 K at the In-
 266 Sight landing site (Plesa et al., 2018). Solar luminosity in the early solar system was as
 267 little as 70% of its present value (Ribas, 2010). To account for this range, we use a sur-
 268 face temperature $T_S = 220 \pm 30 \text{ K}$. We use a crustal density $\rho = 2950 \pm 250 \text{ kg m}^{-3}$,
 269 and the rheological constants as listed in Section 2.1. For each rheology and thermal con-
 270 ductivity, we calculate the necessary heat flux (and its uncertainty) for pore closure as
 271 a function of pore-closure depth. We assume two extremes of crustal heat production:
 272 that of the present day ($47 \pm 3 \text{ pW kg}^{-1}$) and what one might expect of Mars in its ear-
 273 liest days ($290 \pm 40 \text{ pW kg}^{-1}$) (Hahn et al., 2011; Plesa et al., 2018). Results are displayed
 274 in Figure 3.

275 As expected, higher heat fluxes, lower thermal conductivities or weaker rheologies
 276 result in thinner porous layers. For the same given temperature required to close pores
 277 at some depth, a higher crustal heat production will result in a higher surface heat flux.
 278 In turn, this heat flux can be related to a particular time in Martian history. For exam-
 279 ple, to close pores at a depth of 8-11 km requires heat fluxes in excess of 60 mW m^{-2}
 280 for a wet diabase rheology. For dry diabase, the heat fluxes are larger. A larger crustal
 281 heat production (as one would expect early in Mars’ history) will result in a higher sur-
 282 face heat flux when pores closed, but the effect is not significant when closing pores at
 283 shallower depths. Based on the surface heat flux through time resulting from the ther-
 284 mal evolution model of Plesa et al. (2018) plotted in Figure 2a, we conclude that pore
 285 closure must have occurred before 4 Ga and that pore production must have been even
 286 earlier. This conclusion is robust to uncertainties in thermal conductivity, rheology, and
 287 crustal heat production (at least to close pores at $\sim 10 \text{ km}$ depth). Because the employed
 288 thermal evolution model of Plesa et al. (2018) is an upper bound on likely heat fluxes,
 289 this age estimate is conservative and robust to uncertainties in Mars’ initial conditions:
 290 other cases cool to a heat flux of 60 mW m^{-2} earlier in Mars’ history.

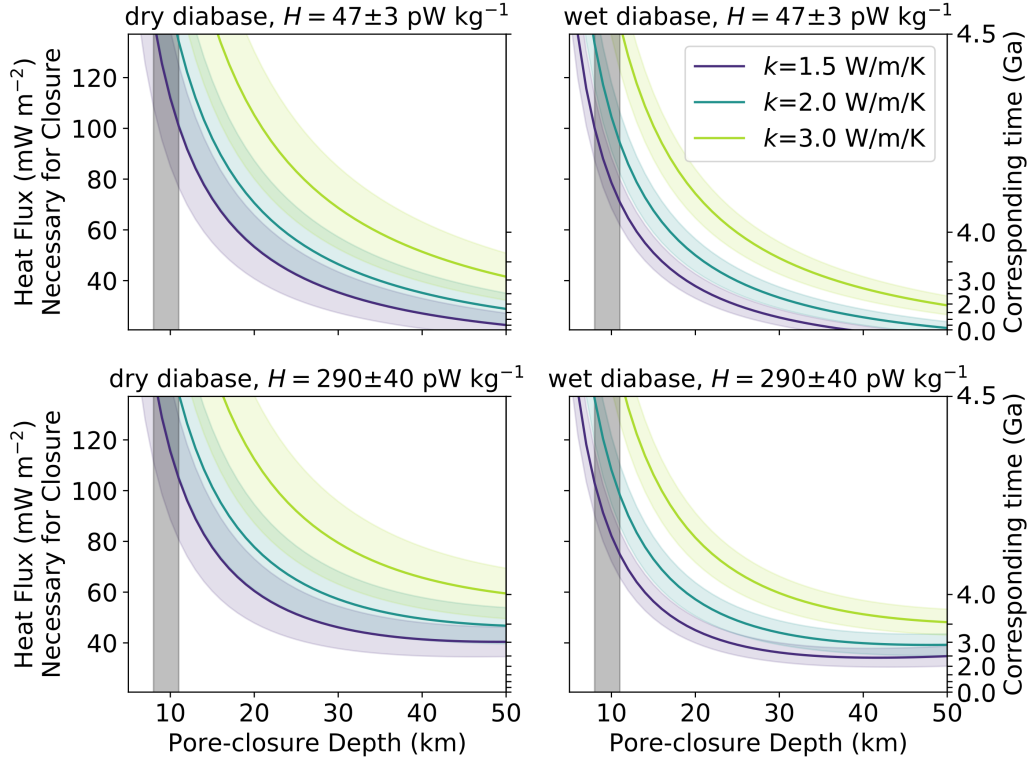


Figure 3. For each rheology and crustal heat production (H) combination, we vary the thermal conductivity to find the necessary surface heat flux needed to close pores viscously as a function of depth (Equation 5), assuming 10 Myr have elapsed to close pores. The secondary y-axis relates the necessary heat flux to the time that heat flux occurred at the InSight landing site according to case 110 of the Plesa et al. (2018) Mars thermal evolution model. The colored shaded regions highlight the corresponding uncertainty for each assumed thermal conductivity. Examining multiple thermal conductivities allows us to ascertain its effect on the maximum heat flux without needing to factor it into the calculation of uncertainty. The vertical grey shaded region highlights the 8-11 km depth at which InSight detects a discontinuity in seismic wave speed.

291 Our constraint can be compared with thermal models and other measurements. For
 292 instance, Hauck and Phillips (2002)'s thermal model predicts a surface heat flux of up
 293 to $\sim 65 \text{ mW m}^{-2}$ before 4 Ga, albeit for an average crustal thickness of 62 km. By ex-
 294 amining the viscous relaxation of craters, Karimi et al. (2016) were able to construct a
 295 map of Mars' surface heat flux during the Noachian, finding a heat flux $\sim 70 \text{ mW m}^{-2}$
 296 near where InSight landed. Both Hauck and Phillips (2002)'s thermal model and Karimi
 297 et al. (2016)'s inversion are consistent with heat fluxes exceeding 60 mW m^{-2} before 4
 298 Ga. Another independent estimate of paleo heat fluxes may be derived from measure-
 299 ments of elastic thickness. For instance, McGovern et al. (2004) find heat fluxes in ex-
 300 cess of 35, 43, 48 and 50 mW m^{-2} for four Noachian terrains. Likewise, Broquet and Wic-
 301 zorek (2019) generally obtain heat fluxes greater than 50 mW m^{-2} for ancient, eroded
 302 volcanoes. Although uncertain, all these estimates are very consistent with our constraint.

303 5 Conclusion

304 This analysis assumes that the porous-to-non-porous transition is the cause of the
 305 seismic wave speed discontinuity detected by InSight (Lognonné et al., 2020). From that
 306 transition depth we conclude that pores formed prior to 4 Ga and in the presence of a
 307 heat flux exceeding 60 mW m^{-2} . If the seismic discontinuity instead marks a different
 308 transition of rock composition and porosity continues to a greater depth, this may in-
 309 dicate a delayed onset of pore-closure until later in Mars' history when it had cooled down.
 310 Alternatively, a Mars that had started off colder would also ensure a smaller heat flux,
 311 resulting in a deeper porous-to-compacted transition. Finally, if the crust has cooled sig-
 312 nificantly, additional layers of sediments or lavas could depress the transition from porous-
 313 to-compacted crust without further closing pores due to the extra overburden pressure.

314 In the future, further seismic events will allow improved estimation of the depth
 315 at which pores close. When such a new measurement is made, the approach we present
 316 in this paper can be used to further clarify the thermal state of the ancient Martian crust.

317 Appendix A Quantifying Uncertainty

318 Equation 5 allows us to determine the maximum heat flux a region experienced as
 319 a function of the depth to pore closure in the crust. However, it also relies on assump-
 320 tions of the rock types that make up the crust, the rheological constants for each rock
 321 type, surface temperature, rock density, thermal conductivity of the rock, and heat pro-
 322 duction within the rock.

323 One can find the uncertainty in maximum heat flux as a function of the uncertain-
 324 ties of each variable:

$$325 \begin{aligned} \delta F_C^2 &= \left(\frac{\partial F_C}{\partial k}\right)^2 \delta k^2 + \left(\frac{\partial F_C}{\partial T_S}\right)^2 \delta T_S^2 + \left(\frac{\partial F_C}{\partial Q}\right)^2 \delta Q^2 + \left(\frac{\partial F_C}{\partial H}\right)^2 \delta H^2 \\ 326 &+ \left(\frac{\partial F_C}{\partial A}\right)^2 \delta A^2 + \left(\frac{\partial F_C}{\partial \rho}\right)^2 \delta \rho^2 + \left(\frac{\partial F_C}{\partial n}\right)^2 \delta n^2. \end{aligned} \quad (\text{A1})$$

327 Taking each partial derivative of Equation 5 and inserting it into Equation A1, we
 328 find the uncertainty to be:

$$329 \begin{aligned} \delta F_C^2 &= F_C^2 \left(\frac{\delta k}{k}\right)^2 + \left(\frac{k}{z}\right)^2 \delta T_S^2 + \left(F_C + \frac{k T_S}{z}\right)^2 \left(\frac{\delta Q}{Q}\right)^2 + \left(\frac{\rho z}{2}\right)^2 \delta H^2 \\ 330 &+ \frac{\left(F_C + \frac{k T_S}{z} - \frac{\rho H z}{2}\right)^2}{\ln\left(\frac{t P^n A}{\ln(\phi_0/\phi_C)}\right)^2} \left[\left(\frac{\delta A}{A}\right)^2 + \left(\frac{n}{\rho} + \frac{H z}{2}\right)^2 \delta \rho^2 + \ln(P)^2 \delta n^2 \right]. \end{aligned} \quad (\text{A2})$$

331 By inspecting Equation A2, one can see that the variables whose individual uncertain-
 332 ties have the largest effect upon the total uncertainty are the thermal conductivity k ,
 333 the surface temperature T_S , and the activation energy Q .

Acknowledgments

We thank Adrien Broquet for his insightful comments on our manuscript. We also thank Walter Kiefer and an anonymous reviewer for their thoughtful and constructive comments. This is InSight contribution number 163. Parts of this work were supported by NASA grant 80NSSC18K1627 to FN. ACP gratefully acknowledges the financial support and endorsement from the DLR Management Board Young Research Group Leader Program and the Executive Board Member for Space Research and Technology. MAW was supported by the French Space Agency (CNES).

Data for the heat flux and temperature as a function of depth of the Martian crust were outputs of the Plesa et al. (2018) 3D Mars thermal evolution model at the InSight landing site. Data for several cases (the conditions of each are detailed in the Supplementary Material of Plesa et al., 2018) are archived in the Dryad repository (https://datadryad.org/stash/share/uS-MKU5VyuUrwsLpidg-qGWFxf_yMvHo1KUxU8wi6qk).

References

- Besserer, J., Nimmo, F., Roberts, J., & Pappalardo, R. (2013). Convection-driven compaction as a possible origin of Enceladus's long wavelength topography. *Journal of Geophysical Research: Planets*, *118*(5), 908–915. doi: 10.1002/jgre.20079
- Besserer, J., Nimmo, F., Wicczorek, M., Weber, R., Kiefer, W., McGovern, P., ... Zuber, M. (2014). GRAIL gravity constraints on the vertical and lateral density structure of the lunar crust. *Geophysical Research Letters*, *41*(16), 5771–5777. doi: 10.1002/2014GL060240
- Bottke, W., & Andrews-Hanna, J. (2017). A post-accretionary lull in large impacts on early Mars. *Nature Geoscience*, *10*, 344–348. doi: 10.1038/ngeo2937
- Broquet, A., & Wicczorek, M. (2019). The gravitational signature of Martian volcanoes. *Journal of Geophysical Research: Planets*, *124*(8), 2054–2086. doi: 10.1029/2019JE005959
- Caristan, Y. (1980). *High temperature mechanical behavior of Maryland diabase* (Unpublished doctoral dissertation). Massachusetts Institute of Technology.
- Clauser, C., & Huenges, E. (1995). Rock physics and phase relations: A handbook of physical constants. In A. Brandt & H. Fernando (Eds.), (Vol. 3, p. 105).
- Clifford, S. (1993). A model for the hydrologic and climatic behavior of water on Mars. *Journal of Geophysical Research: Planets*, *98*(E6), 10973. doi: 10.1029/93JE00225
- Clifford, S., & Parker, T. (2001). The evolution of the Martian hydrosphere: Implications for the fate of a primordial ocean and the current state of the northern plains. *Icarus*, *154*(1), 40 – 79. doi: 10.1006/icar.2001.6671
- Demming, D. (2002). *Introduction to hydrology*. McGraw-Hill.
- Eluszkiewicz, J. (2004). Compaction and internal structure of mimas. *Icarus*, *84*(1), 215. doi: 10.1016/0019-1035(90)90167-8
- Fowler, A. (1985). A mathematical model of magma transport in the asthenosphere. *Geophysical & Astrophysical Fluid Dynamics*, *33*(1–4), 63. doi: 10.1080/03091928508245423
- Gail, H.-P., Henke, S., & Tieloff, M. (2015). Thermal evolution and sintering of chondritic planetesimals ii. improved treatment of the compaction process. *Astronomy & Astrophysics*, *576*(A60). doi: 10.1051/0004-6361/201424278
- Gillet, K., Calvet, M., & Monnereau, M. (2017). Scattering attenuation profile of the moon: Implications for shallow moonquakes and the structure of the megaregolith. *Physics of the Earth and Planetary Interiors*, *262*, 28. doi: 10.1016/j.pepi.2016.11.001
- Golombek, M., Warner, N., Grant, J., Hauber, E., Ansan, V., Weitz, C., ... Banerdt, W. (2020). Geology of the insight landing site on Mars. *Nature Communications*, *11*, 1014. doi: 10.1038/s41467-020-14679-1

- 387 Hahn, B., McLennan, S., & Klein, E. (2011). Martian surface heat production and
388 crustal heat flow from Mars Odyssey gamma-ray spectrometry. *Geophysical*
389 *Research Letters*, *38*(14). doi: 10.1029/2011GL047435
- 390 Hanna, J., & Phillips, R. (2005). Hydrological modeling of the martian crust with
391 application to the pressurization of aquifers. *Journal of Geophysical Research:*
392 *Planets*, *110*(E1). doi: 10.1029/2004JE002330
- 393 Hauck, S., & Phillips, R. (2002). Thermal and crustal evolution of Mars. *Jour-*
394 *nal of Geophysical Research: Planets*, *107*(E7), 6-1 – 6-19. doi: 10.1029/
395 2001JE001801
- 396 Hewitt, D., Neufeld, J., & Lister, J. (2014). High rayleigh number convection in a
397 three-dimensional porous medium. *Journal of Fluid Mechanics*, *748*, 879. doi:
398 10.1017/jfm.2014.216
- 399 Karimi, S., Dombard, A., Buczkowski, D., Robbins, S., & Williams, R. (2016). Using
400 the viscoelastic relaxation of large impact craters to study the thermal history
401 of Mars. *Icarus*, *272*, 102 – 113. doi: 10.1016/j.icarus.2016.02.037
- 402 Kieffer, H. (2013). Thermal model for analysis of Mars infrared mapping. *Jour-*
403 *nal of Geophysical Research: Planets*, *118*(3), 451 – 470. doi: 10.1029/
404 2012JE004164
- 405 Kossacki, K., & Lorenz, R. (1996). Hiding titan’s ocean: Densification and hydrocar-
406 bon storage in an icy regolith. *Planetary and Space Science*, *44*(9), 1029.
- 407 Lewis, K., Peters, S., Gonter, K., Morrison, S., Schmerr, N., Vasavada, A., &
408 Gabriel, T. (2019). A surface gravity traverse on mars indicates low
409 bedrock density at gale crater. *Science*, *363*(6426), 535-537. doi: 10.1126/
410 science.aat0738
- 411 Lognonné, P., Banerdt, W., Pike, W., Giardini, D., Christensen, U., Garcia, R., ...
412 Zweifel, P. (2020). Constraints on the shallow elastic and anelastic struc-
413 ture of mars from insight seismic data. *Nature Geoscience*, *13*, 213. doi:
414 10.1038/s41561-020-0536-y
- 415 Mackwell, S., Zimmerman, M., & Kohlstedt, D. (1998). High-temperature deforma-
416 tion of dry diabase with application to tectonics on venus. *Journal of Geophys-*
417 *ical Research: Solid Earth*, *103*(B1), 975-984. doi: 10.1029/97JB0267
- 418 Manning, C., & Ingebritsen, S. (1999). Permeability of the continental crust: Impli-
419 cations of geothermal data and metamorphic systems. *Reviews of Geophysics*,
420 *37*(1), 127 – 150. doi: 10.1029/1998RG900002
- 421 McGovern, P., Solomon, S., Smith, D., Zuber, M., Simons, M., Wieczorek, M.,
422 ... Head, J. (2004). Correction to “localized gravity/topography ad-
423 mittance and correlation spectra on Mars: Implications for regional and
424 global evolution”. *Journal of Geophysical Research: Planets*, *109*(E7). doi:
425 10.1029/2004JE002286
- 426 Neumann, W., Breuer, D., & Spohn, T. (2015). Modelling the internal structure
427 of Ceres: Coupling of accretion with compaction by creep and implications for
428 the water-rock differentiation. *Astronomy & Astrophysics*, *584*(A117). doi:
429 10.1051/0004-6361/201527083
- 430 Nimmo, F., Pappalardo, R., & Giese, B. (2003). On the origins of band topography,
431 Europa. *Icarus*, *166*(1), 21. doi: 10.1016/j.icarus.2003.08.002
- 432 Ohring, G., & Mariano, J. (1968). Seasonal and latitudinal variations of the average
433 surface temperature and vertical temperature profile on Mars. *Journal of the*
434 *Atmospheric Sciences*, *25*(5), 673-681. doi: 10.1175/1520-0469(1968)025<0673:
435 SALVOT>2.0.CO;2
- 436 Pan, L., Quantin-Nataf, C., Tauzin, B., Michaut, C., Golombek, M., Lognonné,
437 P., ... Lucas, A. (2020). Crust stratigraphy and heterogeneities of the
438 first kilometers at the dichotomy boundary in western Elysium Planitia
439 and implications for InSight lander. *Icarus*, *338*, 113511. doi: 10.1016/
440 j.icarus.2019.113511
- 441 Parmentier, E., & Zuber, M. (2007). Early evolution of Mars with mantle compo-

- 442 sitional stratification or hydrothermal crustal cooling. *Journal of Geophysical*
 443 *Research: Planets*, 112(E2). doi: 10.1029/2005JE002626
- 444 Plesa, A.-C., Padovan, S., Tosi, N., Breuer, D., Grott, M., Wieczorek, M., ...
 445 Banerdt, W. (2018). The thermal state and interior structure of Mars. *Geo-*
 446 *physical Research Letters*, 45(22), 12198. doi: 10.1029/2018GL080728
- 447 Ribas, I. (2010). The sun and stars as the primary energy input in planetary atmo-
 448 spheres. *Proceedings of the International Astronomical Union*, 5(S264), 3 – 18.
 449 doi: 10.1017/S1743921309992298
- 450 Rust, A., Russel, J., & Knight, R. (1999). Dielectric constant as a predictor of
 451 porosity in dry volcanic rocks. *Journal of Volcanology and Geothermal Re-*
 452 *search*, 99(1), 79–96. doi: 10.1016/S0377-0273(99)00055-4
- 453 Schmoker, J., & Gautier, D. (1988). Sandstone porosity as a function of thermal ma-
 454 turity. *Geology*, 16(11), 1007 – 1010. doi: 10.1130/0091-7613(1988)016<1007:
 455 SPAAFO>2.3.CO;2
- 456 Seipold, U. (1998). Temperature dependence of thermal transport properties of crys-
 457 talline rocks: A general law. *Tectonophysics*, 291, 161. doi: 10.1016/S0040-
 458 -1951(98)00037-7
- 459 Smrekar, E., Lognonné, P., Spohn, T., Banerdt, W., Breuer, D., Christensen, U.,
 460 ... Mieczorek, M. (2019). Pre-mission insights on the interior of mars. *Space*
 461 *Science Reviews*, 215, 3. doi: 10.1007/s11214-018-0563-9
- 462 Sun, V., Stack, K., Kah, L., Thompson, L., Fischer, W., Williams, A., ... VanBom-
 463 mel, S. (2019). Late-stage diagenetic concretions in the Murray formation,
 464 Gale crater, Mars. *Icarus*, 321, 866 – 890. doi: 10.1016/j.icarus.2018.12.030
- 465 Wahl, D., Wieczorek, M., Wünnemann, K., & Oberst, J. (2020). Crustal porosity of
 466 lunar impact basins. *Journal of Geophysical Research: Planets*, 125(4). doi: 10
 467 .1029/2019JE006335
- 468 Wieczorek, M., Neumann, G., Nimmo, F., Kiefer, W., Taylor, G., Melosh, H., ...
 469 Zuber, M. (2013). The crust of the Moon as seen by GRAIL. *Science*,
 470 339(6120), 671–675. doi: 10.1126/science.1231530
- 471 Wong, T.-F., & Baud, P. (2012). The brittle-ductile transition in porous rock: A re-
 472 view. *Journal of Structural Geology*, 44, 25 – 53. doi: 10.1016/j.jsg.2012.07
 473 .010